J. Appl. Comput. Mech., 4(2) (2018) 95-104
DOI: 10.22055/JACM.2017.22761.1140

ISSN: 2383-4536
jacm.scu.ac.ir

Shahid Chamran University of Ahvaz

Journal of Applied and Computational Mechanics

Research Article

Study of Parameters Affecting Separation Bubble Size in High Speed Flows using k-ω Turbulence Model

Amjad Ali Pasha

Assistant Professor, Department of Aeronautical Engineering, King Abdul Aziz University, Jeddah- 21589, Saudi Arabia

Received July 13 2017; Revised August 06 2017; Accepted for publication August 15 2017.
Corresponding author: Amjad Ali Pasha, aapasha@kau.edu.sa

Abstract. Shock waves generated at different parts of vehicle interact with the boundary layer over the surface at high Mach flows. The adverse pressure gradient across strong shock wave causes the flow to separate and peak loads are generated at separation and reattachment points. The size of separation bubble in the shock boundary layer interaction flows depends on various parameters. Reynolds-averaged Navier-Stokes equations using the standard two-equation k-ω turbulence model is used in simulations for hypersonic flows over compression corner. Different deflection angles, including θ ranging from 15^o to 38^o, are simulated at Mach 9.22 to study its effect on separated flow. This is followed by a variation in the Reynolds number based on the boundary layer thickness, Re_δ from $1x10^5$ to $4x10^5$. Simulations at different constant wall conditions T_w of cool, adiabatic, and hot are also performed. Finally, the effect of free stream Mach numbers M_∞, ranging from 5 to 9, on interaction region is studied. It is observed that an increase in parameters, θ, Re_δ, and T_w results in an increase in the separation bubble length, L_s, and an increase in M_∞ results in the decrease in L_s.

Keywords: High speed flows, Shock/boundary-layer interaction, Hypersonic flows, Shock-waves, Boundary-layer, Compression corner, Computational fluid dynamics.

1. Introduction

Shock wave/boundary layer interactions can induce separation, which causes loss of control surface effectiveness, drop of air intake efficiency and may be at the origin of large scale fluctuations such as air-intake buzz, buffeting or fluctuating side loads in separated propulsive nozzles and reentry vehicles. In high enthalpy flows, the subsequent reattachment on a nearby surface of the separated shear layer gives rise to the local peak wall pressure, the skin friction and heat transfer rates which can be far in excess as compared to the attached boundary layer [1].

During its flight, a hypersonic vehicle covers a wide range of conditions (at different angles of attack) from low to high Mach numbers at different Reynolds flows and wall temperatures [2]. The flow separation, often associated with shock wave/boundary layer interactions, generally leads to increased energy losses in the system and degrades the performance of the aerodynamic device [3]. The flow unsteadiness, often a result of separation, can cause additional problems which is undesirable in practice [4-8]. The effect of parameters like deflection angle, Reynolds number, wall temperature, and Mach number on the flow separation is beneficial to improve the design of the device under consideration [1, 9-12].

The flow separation resulting from shock boundary layer interactions not only cause localized loads but also influence aerodynamics of the vehicle. Predicting shock wave/boundary layer interactions and understanding how to control them is a critical technology area to develop propulsion systems for supersonic and hypersonic vehicles [13]. A large number of experimental and numerical results on shock wave/boundary layer interactions in two-dimensional flows have allowed a clear identification of the role played by the main parameters involved in the interaction process [14-16]. Moreover, correlation laws have been deduced giving the upstream interaction length, the limit for shock induced separation for high-speed flows [17-19].

Published Online: January 05 2018

CFD studies have been performed experimentally to observe the wall temperature and the leading edge nose radius on shock boundary layer interactions in double compression corner flows. It is observed that these parameters have a remarkable influence on the size of separation bubble [20-22]. Besides, as the constant wall temperature is increased from 300 to 760 K, the separation bubble size increases and peak values of the heat transfer rate is observed in the reattachment region for larger flow separation. It is also demonstrated that high Reynolds flows (turbulent case) do not exhibit boundary layer separation due to the higher momentum within the boundary layer as compared to low Reynolds flows laminar cases which show flow separation [22]. Moreover, it is observed that higher deflection angles lead to a larger separation bubble size due to the increased pressure rise across shock waves [11-12].

The large eddy simulation (LES) and direct numerical simulation (DNS) require large computational time and resources; they are still difficult to be applied in engineering practically, especially for high Reynolds and high Mach flows [23]. As a practical approach, Reynolds-averaged Navier-Stokes (RANS) equations along with turbulence models are used to compute hypersonic flows which are used in the design of aerospace vehicles [24-32].

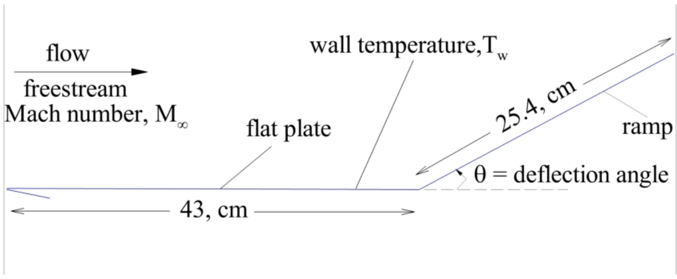

Fig. 1. Geometry details of compression corner.

A supersonic and hypersonic flow over a compression corner occurs in a super/hypersonic aircraft, scramjets and re-entry vehicles. The aim is to numerically simulate hypersonic flows for Elstrom [33] compression corner configurations as indicated in Fig. 1. The geometry consists of a flat plate of length = 43 cm followed by a ramp of length = 25.4 cm, inclined to it at a certain deflection angle. The perfect gas assumption is applicable due to the low stagnation enthalpy. Nitrogen gas is taken as a working fluid. Various ramp deflection angles, Reynolds numbers, wall temperatures, and Mach numbers are employed to simulate and gather data from incipient separation to separated flows as shown in Tables 1-4. This study focuses on the use of computational fluid dynamics (CFD) as a tool to study the effect of these parameters on the separation bubble size and its effect on the flow field and the peak loads generated at separation and reattachment regions.

This paper is organized as follows: First, the simulation methodology and test cases are described. Next, the CFD results for different cases are discussed in terms of mean flow field variables, property profiles, surface pressure, skin friction, and separation bubble length. Finally, conclusions are discussed briefly.

2. Simulation Methodology

We solve the two-dimensional Favre-averaged Navier-Stokes equations for the mean flow, as presented by Wilcox [34]. The code of Sinha et al. [35] is used in the simulations which is capable of running on parallel machines. The standard two-equation k-ω model [36] is used in the simulations without any compressibility corrections. The governing equations are discretized in a finite volume formulation where the inviscid fluxes are computed using a modified low-dissipation form of the Steger-Warming flux splitting approach [37]. The turbulence model equations are fully coupled to the mean flow equations. The method is second order accurate both in stream-wise and wall normal directions. The implicit method of Wright et al. [38] is used to integrate in time and to reach a steady-state solution. The code has been used in several supersonic and hypersonic applications [39-41].

A structured Cartesian mesh with exponential stretching normal to the wall is used to span the computational domain. The grid points are clustered at the corner. Following Menter [42], the free stream conditions for standard k-ω models used in the simulations are $\omega_\infty = U_\infty / L$ and $k_\infty = 0.01\ \nu_\infty\ \omega_\infty$, where ν is the kinematic viscosity, U_∞ is the free stream velocity, and L = 1 m is a characteristic length. No-slip and zero normal pressure gradients are applied at the wall. An extrapolation boundary condition is assigned at top and exit planes. For the turbulence quantities, the boundary conditions at the wall [42] are taken as k = 0 and $\omega = 60\nu_w / \beta_1/\Delta y_1^2$, where $\beta_1 = 3/40$ and Δy_1 is the normal distance to the grid point nearest to the wall. Based on the grid convergence study, a grid size of 500 x 400 is used in the simulations. The wall normal spacing of one micron is used in the simulations and the wall unit of $y^2+ < 1.8$ is obtained in the whole domain. Moreover, CFL numbers up to 50 are used in the computations.

Table 1. Variation of defection angles θ

Case-1	
Deflection angles	38°, 34°, 30°, 15°
Free stream Mach number M_∞	9.22
Free stream temperature T_∞ (K)	59.4
Free stream pressure P_∞ (kPa)	2.3
Reynolds number Re_δ, x 10^5	4
Ratio of wall to recovery temperature, T_w/T_r	0.3

Table 2. Variation of Reynolds number based on upstream boundary layer thickness, Re_δ

Case-2	
Deflection angle	38°
Free stream Mach number M_∞	9.22
Free stream temperature T_∞ (K)	59.4
Free stream pressure P_∞ (kPa)	2.3
Reynolds number Re_δ, x 10^5	4, 2, 1
Ratio of wall to recovery temperature, T_w/T_r	0.3

Table 3. Variation of constant wall temperature, T_w

Case-3	
Deflection angle	38°
Free stream Mach number M_∞	9.22
Free stream temperature T_∞, (K)	59.4
Free stream pressure P_∞, (kPa)	2.3
Unit Reynolds number $Re_{1\infty}$, x 10^6, m^{-1}	47
Ratio of wall to recovery temperature, T_w/T_r	0.3, 0.5,0.7, 1.0, 1.2

Table 4. Variation of Mach number, M_∞

Case-4	
Deflection angle	38°
Free stream Mach numbers M_∞	9.22, 8.2, 7.3, 5
Free stream temperature T_∞, (K)	59.4
Free stream pressure P_∞ (kPa)	2.3
Unit Reynolds number $Re_{1\infty}$, x 10^6 (m^{-1})	47
Ratio of wall to recovery temperature, T_w/T_r	0.3

3. CFD Results

3.1 Case-1: Effect of deflection angles

CFD results of case-1 are shown in Fig. 2 for compression corner configuration in terms of normalized pressure contours (Table 1). Different deflection angles ranging from 15° to 38° at Mach 9.22 are simulated and the cool wall (T_w/T_r=0.3) temperature is taken with a constant surface temperature of 295 K. The boundary layer separates to a larger extent for the strongest interaction case with deflection angle of 38° due to a higher adverse pressure gradient developed across the oblique shock wave at the corner. The inviscid structure of the inclined oblique shock wave at the corner is modified due to viscous effects. The flow separates at separation point, S, and reattaches at reattachment point, R. The flow field comprises of separation shock, separation bubble, weak compression waves and reattachment shock. The weakest interaction case with a deflection angle of 15° shows incipient flow separation at the corner.

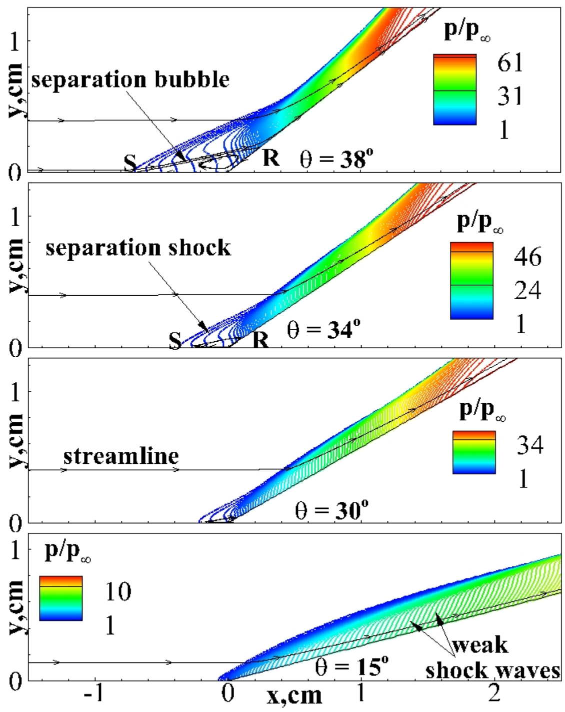

Fig. 2. Distribution of computed normalized pressure at different deflection angles of 38°, 34°, 30°, and 15° for the compression ramp flow at Mach 9.22, Re_δ = 4x10^5, and T_w/T_r = 0.3.

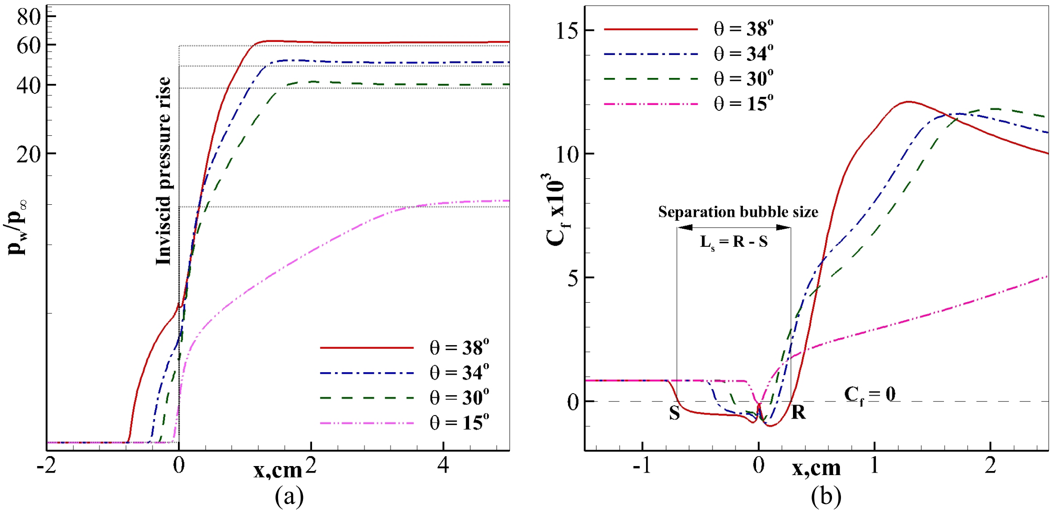

Fig. 3. Computed (a) wall pressure (b) skin-friction with deflection angles of 38°, 34°, 30°, and 15° at Mach 9.22, Re_δ = 4x10^5, and T_w/T_r = 0.3.

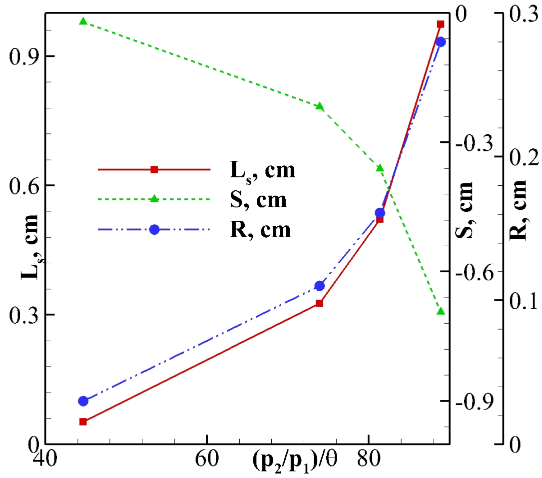

Fig. 4. Computed separation bubble size, L_s, separation point, S and reattachment point, R locations with deflection angles, θ = 38°, 34°, 30°, and 15° normalized with inviscid pressure ratio, (p_2/p_1) across shock.

The normalized wall pressure variation in Fig. 3a shows that as the inviscid pressure rise increases across the oblique shock wave for higher angles, the separation point shifts upstream. The origin is located at the junction of the plate and ramp of the compression corner. The wall pressure rises at separation region, S, develops a plateau in the separation region, and shoots to large values in the reattachment region, R. The pressure downstream of the corner is higher than the inviscid pressure due to the flow passing through multiple compression waves. The separation bubble size, L_s = (R – S) cm, is calculated based on the distance between the separation point location, S cm, and the reattachment point location, R cm. The skin friction, C_f, becomes zero for two-dimensional flows at these points and is marked in skin friction plot, C_f, as shown in Fig. 3b. A peak value of skin friction is observed in the reattachment region. Figure 4 shows that L_s varies nonlinearly with parameter $(p_2/p_1)/\theta$. Here, 1 and 2 correspond to upstream and downstream conditions and θ is the deflection angle in radians. Besides, L_s increases by 50% from θ = 34° to 38°.

3.2 Case-2: Effect of Reynolds number

In this case study, the compression corner flow is simulated at Mach 9.22 with the deflection angle of 38° and T_w/T_r = 0.3 (Table 2). The Reynolds number is decreased successively by 50% from Re_δ = 4x10^5 to 1x10^5. This is achieved by reducing the plate length to half, successively upstream of compression corner. For the same Mach flow, as the length is reduced, the boundary layer thickness reduces upstream of the shock boundary layer interaction as shown in Fig. 5. The separation point shifts downstream from higher to lower Re_δ, thereby reducing the separation bubble length, L_s, as shown in Fig. 6. A peak value of the wall pressure is observed for low values of Re_δ = 1x10^5 at the reattachment region, R. Moreover, the skin friction predicts peak values at R due to higher velocity gradients. Thus, we conclude that the boundary layer thickness affects the shock boundary layer interaction region. A reduction in the boundary layer, therefore, results in a reduction of the separation bubble length, L_s, as shown in Fig. 7. The variation of L_s with Re_δ is almost linear and more computations are required to simulate flows for a wide range of Re_δ to predict the actual profile.

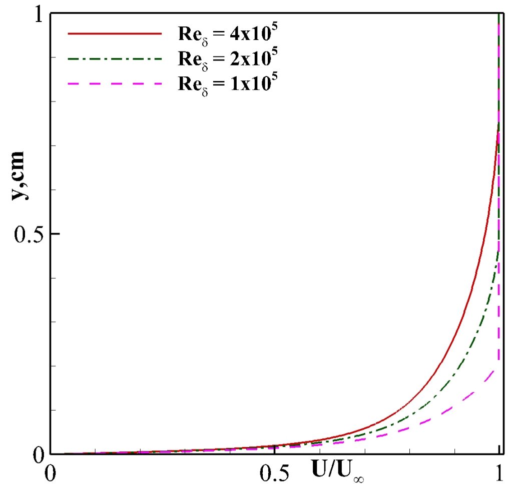

Fig. 5. Computed velocity profiles upstream of shock boundary layer interaction region, with deflection angle of 38° at Mach 9.22, T_w/T_r = 0.3, and different Re_δ = 4x10^5, 2x10^5 and 1x10^5.

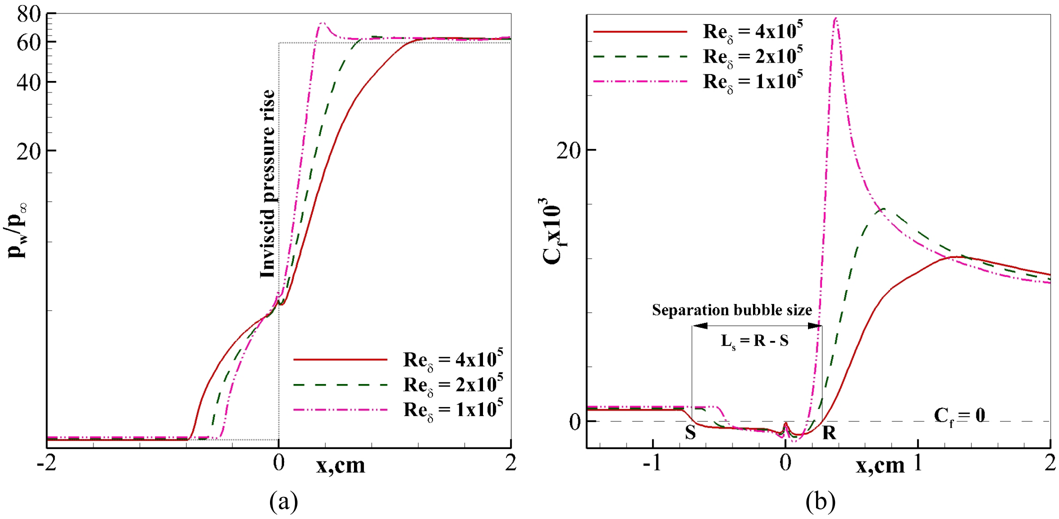

Fig. 6. Computed (a) wall pressure (b) skin-friction with deflection angle of 38° at Mach 9.22, T_w/T_r = 0.3, and different Re_δ of 4x10^5, 2x10^5 and 1x10^5.

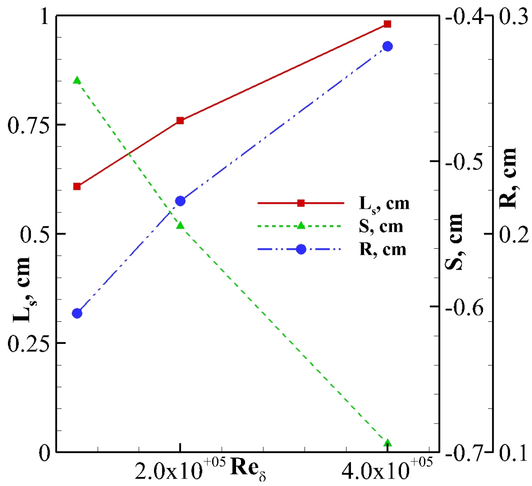

Fig. 7. Computed separation bubble size, L_s, separation point, S, and reattachment point, R locations with deflection angle of 38° at Mach 9.22, T_w/T_r = 0.3, and different Re_δ of 4x10^5, 2x10^5 and 1x10^5.

3.3 Case-3: Effect of wall temperature

In this case study, the flow is simulated for Mach 9.22 flow over the compression corner flow with a ramp angle of 38°, Re_δ = 4x10^5, and different T_w/T_r of 1.2, 1.0, 0.7, 0.5, and 0.3 (see Table 3). The wall temperature is varied from 1200 K to 295 K for these values of T_w/T_r from 1.2 to 0.3. The Fig.8 shows normalized temperature contours for different values of wall temperatures where the extent of separation bubble resulting from shock boundary layer interactions is depicted by separation, S, and the reattachment point, R. In high speed flows, cool and hot walls are defined with respect to the recovery wall temperature. When the wall temperature is less than the recovery wall temperature ($T_w < T_r$), it is called a cool wall, when it is greater than the recovery wall temperature ($T_w > T_r$), it is called a hot wall and when they both are equal ($T_w = T_r$), it is called an adiabatic wall. As the wall becomes cool from T_w/T_r = 1.2 to 0.3, the extent of separation bubble size becomes smaller. This trend is clearly observed in the shifting of separation point, S, downstream in wall pressure variation and skin friction plots as depicted in Fig. 9. It is observed that the peak value of the wall pressure and the skin friction at the reattachment point, R, increases as the wall becomes hotter.

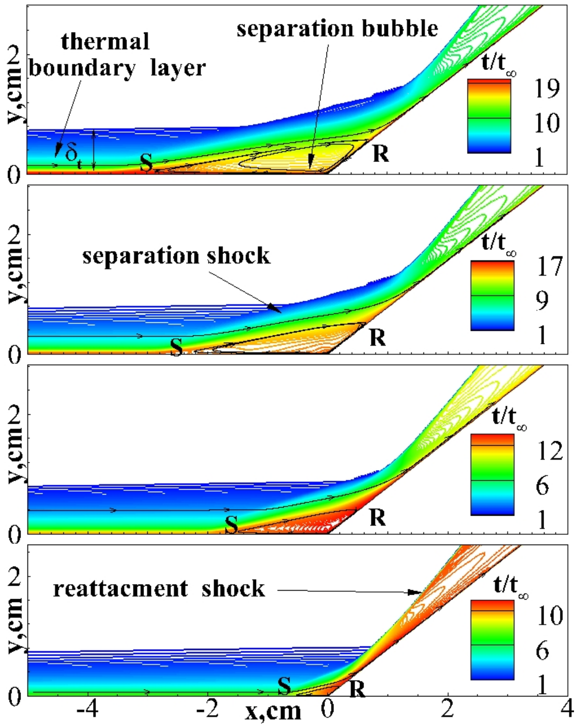

Fig. 8. Distribution of computed normalized temperature at deflection angle of 38° at Mach 9.22, $Re_\delta = 4x10^5$, and T_w/T_r = 1.2, 1.0, 0.7, 0.5, and 0.3.

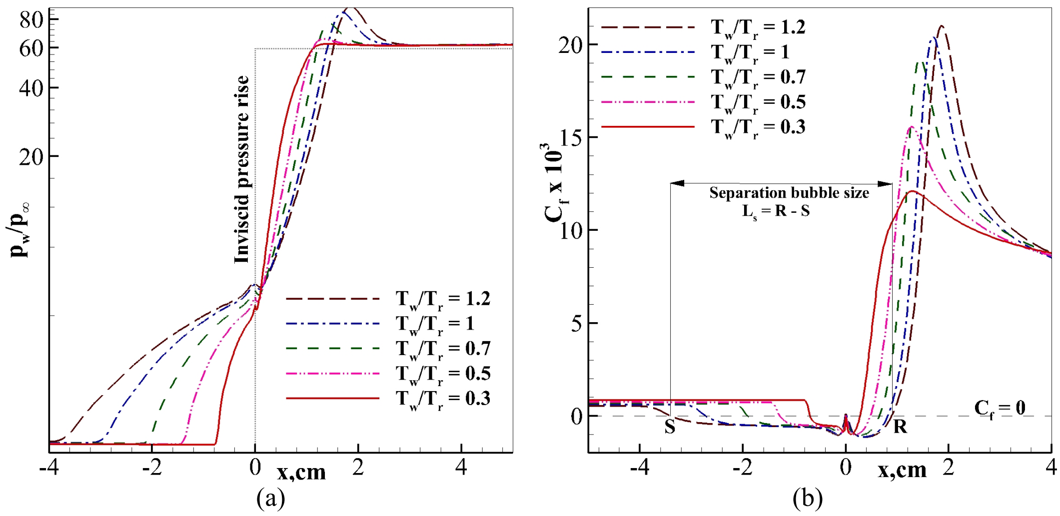

Fig. 9. Computed (a) wall pressure (b) skin-friction with deflection angle of 38° at Mach 9.22, $Re_\delta = 4x10^5$, and different T_w/T_r of 1.2, 1.0, 0.7, 0.5, and 0.3.

When the wall temperature is reduced from 1200 K to 295 K (corresponding to T_w/T_r = 1.2 to 0.3), the temperature near the wall decreases. This results in an increase in the density near the wall to maintain the constant pressure condition across the boundary layer. As shown in Fig.10a, the increase in density results in an increase in the local Reynolds number making the flow more turbulent, hence, making the velocity profiles fuller for cooler walls (see Fig. 10b). These higher velocities for cooler walls in the boundary layer results in a higher momentum, hence, can overcome the pressure gradient across the shock wave and shifts the separation point, S, downstream as shown in Fig. and thereby results in smaller separation bubble length, L_s. Figure 11 shows that the separation bubble length, L_s, and the separation point location varies linearly for a range of T_w/T_r from 1.2 to 0.3, whereas the reattachment point location varies nonlinearly. L_s increases by 4 times when the wall temperature is increased by 4 times from 295 K to 1200 K.

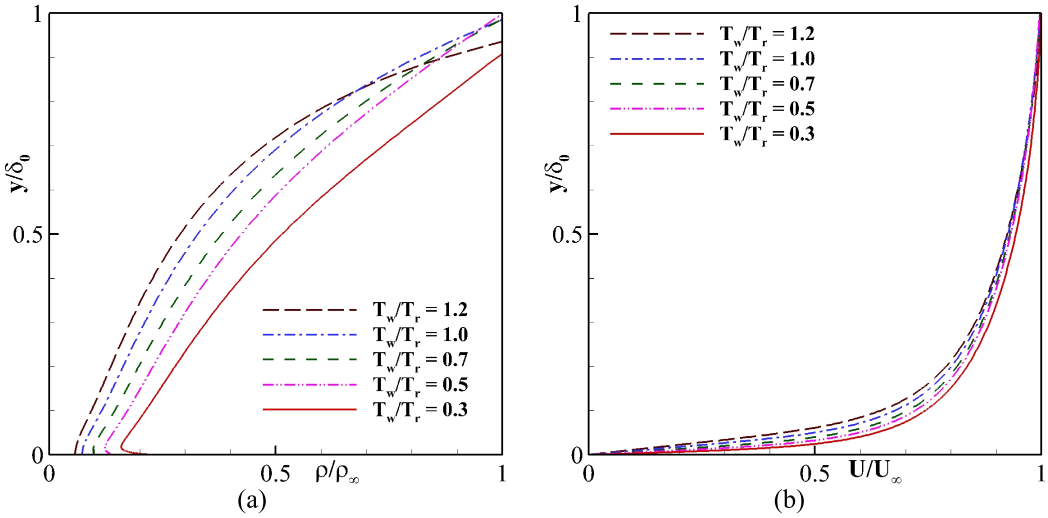

Fig. 10. Computed (a) density and (b) velocity profiles, upstream of shock boundary layer interaction region at location x =-4 cm for Mach 9.22 flow over ramp with deflection angle 38º at T_w/T_r of 1.2, 1.0, 0.7, 0.5, and 0.3.

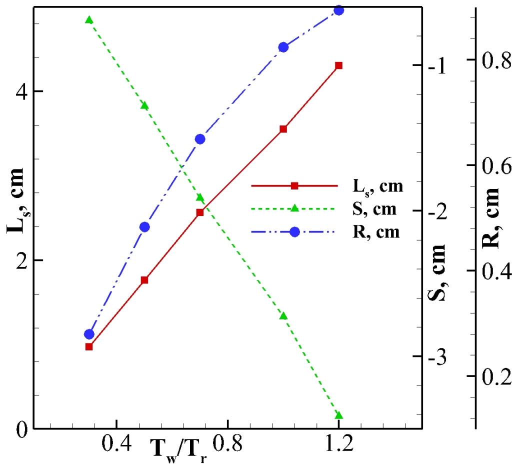

Fig. 11. Computed separation bubble size, L_s, separation point, S, and reattachment point, R, locations with deflection angle of 38º at Mach 9.22, $Re_\delta = 4x10^5$, and different T_w/T_r of 1.2, 0.7, 0.5, 1.0, and 0.3.

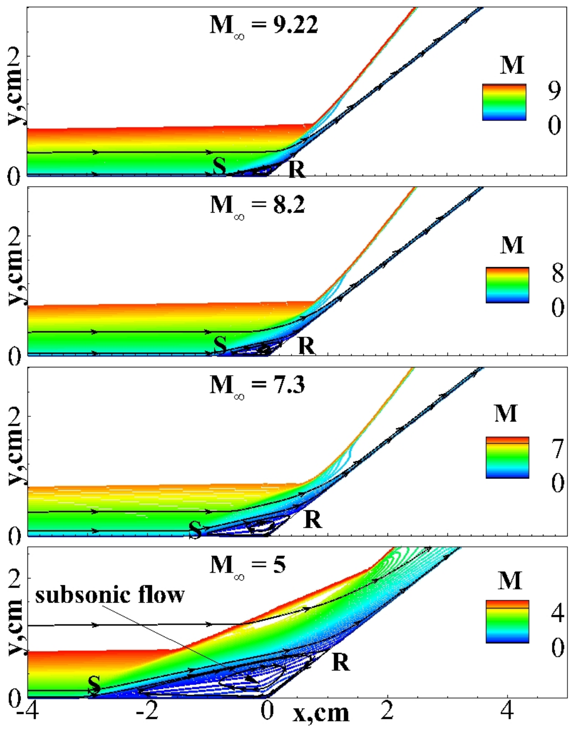

Fig. 12. Distribution of computed Mach number at deflection angle of 38º, $Re_\delta = 4x10^5$, $T_w/T_r = 0.3$ and different free stream Mach numbers of 9.22, 8.2, 7.3, and 5.

3.4 Case-4: Effect of Mach number

Figure 12 shows CFD results for the flow over the compression ramp with deflection angle 38°, $Re_\delta = 4x10^5$, $T_w/T_r = 0.3$ and varying Mach numbers (see Table 4). The shock strength measured as a ratio of inviscid pressure rise across the oblique shock wave increases from Mach 5 to 9.22. Though the adverse pressure gradient increases across the shock wave and across the upstream boundary layer, it has a little effect on the separation bubble size. The separation point, S, shifts upstream and increases the separation shock length as the Mach number is decreased from 9.22 to 5. It is because lower Mach numbers generate lower values of turbulent kinetic energies, k, hence, lower turbulent Mach numbers, M_t, upstream of the shock boundary layer interaction region as shown in Fig. 13. Lower levels of turbulence cause the flow to separate earlier across the oblique shock for lower Mach numbers. This causes shifting of the initial pressure rise location upstream when Mach number is decreased from 9.22 to 5 as shown in Fig. 14a. At the same time, the reattachment point, R, shifts downstream as shown in Fig. 14b, thereby, increases the length of the separation bubble. The wall pressure at the reattachment region is found to increase as the Mach number decreases. The peak value of the skin friction at the reattachment region increases from Mach 9.22 to 8.2 and then decreases to Mach 5. More investigations are required to understand this behavior. Fig. 15 shows a nonlinear decrease in the separation bubble length with a decrease in the Mach number. The separation and reattachment points also show a nonlinear variation.

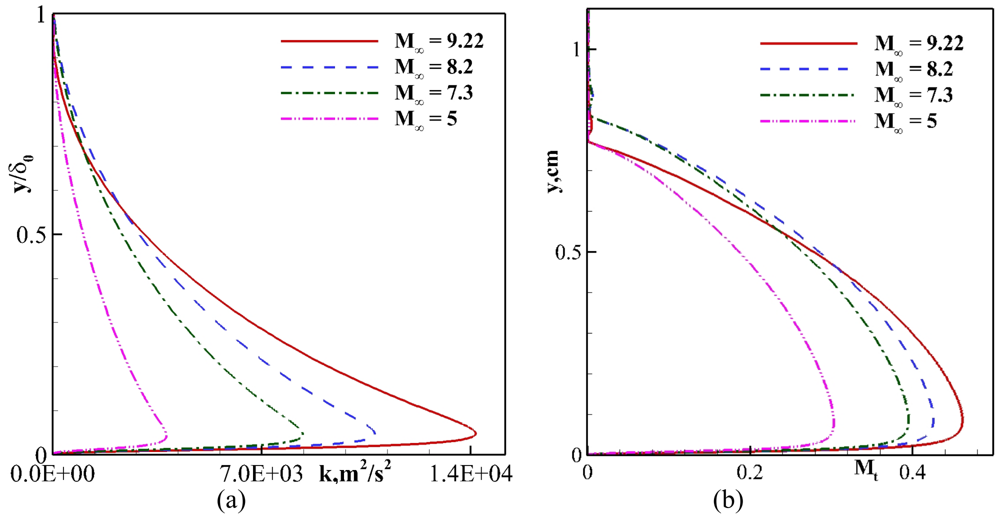

Fig. 13. Computed (a) turbulent kinetic energy, k, and (b) turbulent Mach number, M_t, profiles, upstream of shock boundary layer interaction region with $\theta = 38^o$, $Re_\delta = 4x10^5$, $T_w/T_r = 0.3$ and different free stream Mach numbers M_∞ = 9.22, 8.2, 7.3, and 5.

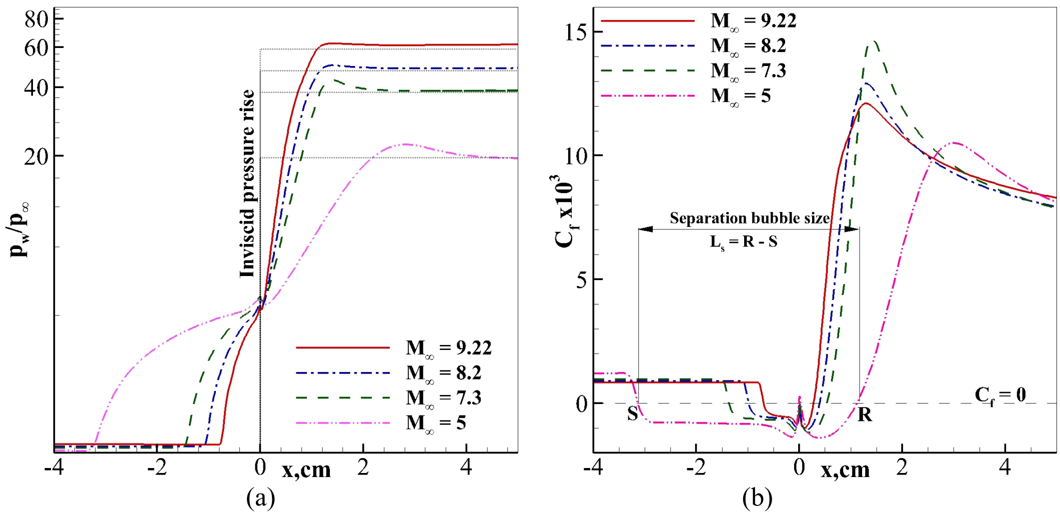

Fig. 14. Computed (a) wall pressure (b) skin-friction with $\theta = 38^o$, $Re_\delta = 4x10^5$, $T_w/T_r = 0.3$ and different M_∞=9.22, 8.2, 7.3, and 5.

4. Conclusion

In this study, CFD is used as a tool to study the effect of the deflection angle, the Reynolds number, the wall temperature, and the Mach number on the separation bubble size in hypersonic shock-wave/turbulent boundary-layer interaction flows. RANS equations using the standard k-ω model is applied in simulations. The flow field in the interaction region, upstream property profiles, surface properties and variation of the separation bubble length are discussed in detail. The results are summarized as follows:

1. For the same free stream Mach number, wall temperature, and Reynolds number, an increase in deflection angle increase the length of the separation bubble nonlinearly. A larger separation bubble results in a peak skin friction at the reattachment

region.

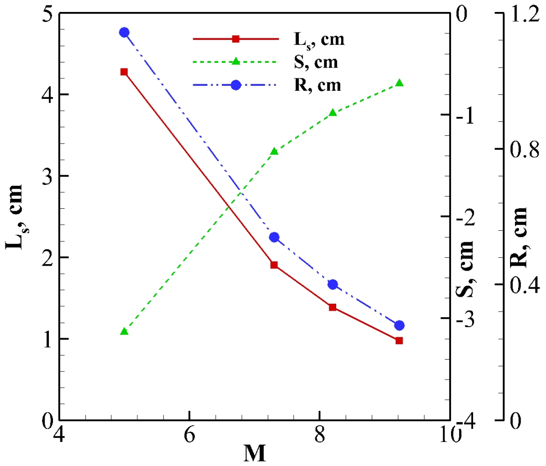

Fig. 15. Computed separation bubble size, L_s, separation point, S, and reattachment point, R, locations with deflection angle of 38°, Re_δ = 4x10^5, T_w/T_r = 0.3 for different free stream Mach numbers of 9.22, 8.2, 7.3, and 5.

2. For the same free stream Mach number, wall temperature, and deflection angle, a decrease in Reynolds numbers give the smaller length of the separation bubble. Peak values of the wall pressure and the skin friction are observed at the reattachment region for low Reynolds flows in the turbulent regime.

3. For the same free stream Mach number, deflection angle, and Reynolds number, an increase in the wall temperature results in a larger length of the separation bubble. This variation is linear. Peak values of the wall pressure and the skin friction are observed at the reattachment region for hotter walls.

4. For the same deflection angle, wall temperature, and Reynolds number, a decrease in the free stream Mach number results in a larger length of the separation bubble. This variation is nonlinear. Peak values of the skin friction are observed at the reattachment region for lower Mach numbers.

Acknowledgments

The author would like to thank to the dean of King Abdul Aziz University and high performance center staff for providing the Aziz supercomputing facility to perform numerical simulations.

Nomenclature

C_f	Skin-friction coefficient	P	Pressure [N/m^2]
k	Turbulent kinetic energy [m^2/s^2]	δ	Boundary-layer thickness upstream of interaction [m]
L_s	Length of separation bubble [m]	θ	Compression corner deflection angle [^{0}]
R	Reattachment point location	ρ	Density [kg/m^3]
S	Separation point location	ω	Turbulent specific dissipation rate [s^{-1}]
T_r	Recovery temperature [K]	w	Wall condition
T_w	Constant wall temperature [K]	∞	Freestream condition
M	Mach number	*CFD*	Computational fluid dynamics
M_t	Turbulent Mach number		

References

[1] Babinsky, H., Harvey, J. K., *Shock Wave-Boundary Layer Interactions*, Cambridge University Press, 2011.

[2] Bose, D., Brown, J. L., Prabhu, D. K., Gnoffo, P., Johnston, C. O., Hollis, B., Uncertainty Assessment of Hypersonic Aerothermodynamics Prediction Capability, *Journal of Spacecraft and Rockets*, 50(1), 2013, pp. 12-18.

[3] DeBonis, J. R., Oberkampf, W. L., Wolf, R. T., Orkwis, P. D., Turner, M. G., Babinsky, H., and Benek, J. A., Assessment of Computational Fluid Dynamics and Experimental Data for Shock Boundary-Layer Interactions, *AIAA Journal*, 50(4), 2012, pp. 891-903.

[4] Sinha, K., Mahesh, K., Candler, G. V., Modeling Shock-Unsteadiness in Shock/Turbulence Interaction, *Physics of Fluids*, 15(8), 2003, pp. 2290-2297.

[5] Verma, S. B., Stark, R., Haid, O., Relation Between Shock Unsteadiness and the Origin of Side-Loads Inside a Thrust Optimized Parabolic Rocket Nozzle, *Aerospace Science and Technology*, 10(6), 2006, pp. 474-483.

[6] Dussauge, J. P., Dupont, P., Debieve, J. F., Unsteadiness in Shock Wave Boundary layer Interactions with Separation, *Progress in Aerospace Sciences*, 10(2), 2006, pp. 85-91.

[7] Estruch, D., Lawson, N. J., MacManus, D. G., Garry, K. P., Stollery, J. L., Measurement of Shock Wave Unsteadiness using a High-Speed Schlieren System and Digital Image Processing, *Review of Scientific Instruments*, 79(12), 2008, pp. 126108.

[8] Clemens, N. T., Narayanaswamy, V., Low-Frequency Unsteadiness of Shock Wave/Turbulent Boundary Layer Interactions, *Annual Review of Fluid Mechanics*, 46, 2014, pp. 469-492.

[9] Bertin, J. J., Hypersonic Aerothermodynamics, *AIAA Education Series*, AIAA, Washington, DC, 1994.
[10] Anderson, J. D., Hypersonic and High Temperature Gas Dynamics, *AIAA*, 2006.
[11] Holden, M. S., Wadhams, T. P., A Database of Aerothermal Measurements in Hypersonic. Flow in "Building Block" Experiments for CFD Validation, *41st Aerospace Sciences Meeting and Exhibit*, 6-9 July 2003, Reno, Nevada, 2003.
[12] Marvin, J. G., Brown, J. L., Gnoffo, P. A., Experimental Database with Baseline CFD Solutions: 2-D and Axisymmetric Hypersonic Shock-Wave/Turbulent-Boundary-Layer Interactions, *NASA/TM–2013–216604*, 2013.
[13] Narayanaswamy, V., Raja, L. L., Clemens, N. T., Control of Unsteadiness of a Shock Wave/Turbulent Boundary Layer Interaction by using a Pulsed-Plasma-Jet Actuator, *Physics of Fluids*, 24(7), 2012, p. 076101.
[14] Delery, J., Marvin, J. G., Shock-Wave Boundary Layer Interactions, edited by E. Reshotko, *AGARD No. 280*, 1986.
[15] Settles, G. S., Dodson, L. J., Supersonic and Hypersonic Shock/Boundary Layer Interaction Data Base, *AIAA Journal*, 32(7), 1994, pp. 1337-1383.
[16] Arnal, D., Delery, J. M., Laminar-Turbulent Transition And Shock-Wave/Boundary-Layer Interaction, *RTO-EN-AVT-116*, Chapter 4, 2004, p. 46.
[17] Ostlund, J., Klingmann, B. M., Supersonic Flow Separation with Application to Rocket Engine Nozzles, *Applied Mechanics Reviews*, 58, 2005, pp. 143-177.
[18] John, B., Kulkarni, V., Effect of Leading Edge Bluntness on the Interaction of Ramp Induced Shock Wave with Laminar Boundary Layer at Hypersonic Speed, *Computers and Fluids*, 96, 2014, pp. 177-190.
[19] Sriram , R., Srinath, L., Manoj, K., Devaraj, K., Jagadeesh, G., On the Length Scales of Hypersonic Shock-Induced Large Separation Bubbles Near Leading Edges, *Journal of Fluid Mechanics*, 806, 2016, pp. 304-355.
[20] Neuenhahm T, Olivier H., Influence of the Wall Temperature and Entropy Layer Effects on Double Wedge Shock Boundary Layer Interactions, *14th AIAA/AHI Space Planes and Hypersonic Systems and Technologies Conference, International Space Planes and Hypersonic Systems and Technologies Conferences*, 2006-8136, 2006.
[21] Brown, L., Fischer, C., Boyce, R. R., Reinartz, B., Olivier, H., Computational Studies of the Effect of Wall Temperature on Hypersonic Shock-Induced Boundary Layer Separation, *Shock Waves*, *In: Hannemann K., Seiler F. (eds) Shock Waves. Springer, Berlin, Heidelberg*, 2009.
[22] Xiaodong, Z., Zhenghong, G., A Numerical Research on a Compressibility-correlated Langtry's Transition Model for Double Wedge Boundary Layer Flows, *Chinese Journal of Aeronautics*, 24, 2011, pp. 249-257.
[23] Yang Z., Large-Eddy Simulation: Past, Present and the Future, *Chinese Journal of Aeronautics*, 28(1), 2015, pp. 11-24.
[24] Knight, D. D., Degrez, G., Shock Wave Turbulent Boundary Layer Interactions In High Mach Number Flows a Critical Survey of Current Numerical Prediction Capabilities, *AGARD Advisory Report*, 319(2), 1998, pp. 1-35.
[25] Knight, D., Yan, H., Panaras, A. G., Zheltovodov, A., Advances in CFD Prediction of Shock Wave Turbulent Boundary Layer Interactions, *Progress in Aerospace Sciences*, 39(2-3), 2003, pp. 121-184.
[26] Roy, C. J., Blottner, F. G., Review and Assessment of Turbulence Models for Hypersonic Flows, *Progress in Aerospace Sciences,* 42(7-8), 2006, pp. 469-530.
[27] Guohua, T. U., Xiaogang, D., Assessment of Two Turbulence Models and Some Compressibility Corrections for Hypersonic Compression Corners by High-Order Difference Schemes, *Chinese Journal of Aeronautics*, 25, 2012, pp. 25-32.
[28] Rui, Z., Chao, Y., Jian, Y., Xinliang, L., Improvement of Baldwin-Lomax Turbulence Model for Supersonic Complex Flows, *Chinese Journal of Aeronautics*, 26(3), 2013, pp. 529-534.
[29] Li, M., Lipeng, L. , Jian, F., Qiuhui, W., A Study on Turbulence Transportation and Modification of Spalart-Allmaras Model for Shock-Wave/Turbulent Boundary Layer Interaction Flow, *Chinese Journal of Aeronautics*, 27(2), 2014, pp. 200-209.
[30] Georgiadis, N. J., Yoder, D. A., Vyas, M. A., Engblom, W. A., Status Of Turbulence Modeling For Hypersonic Propulsion Flow paths, *Theoretical and Computational Fluid Dynamics*, 28(3), 2014, pp. 295-318.
[31] Panaras, A. G., Turbulence Modeling of Flows with Extensive Cross Flow Separation, *Aerospace*, 2, 2015, pp. 461-481.
[32] Gaitonde, D. V., Progress in Shock Wave/Boundary Layer Interactions, *Progress in Aerospace Sciences*, 72, 2015, pp. 80-99.
[33] Elfstrom, G. M., Turbulent Hypersonic Flow at a Wedge- Compression Corner, *Journal of Fluid Mec*hanics, 53(1), 1972, pp. 113-127.
[34] Wilcox, D. C., Turbulence Modeling for CFD, *La Canada CA: 2nd edition*, DCW Industries, 2000.
[35] Sinha, K., Candler, G. V., Convergence Improvement of Two Equation Turbulence Model Calculations, *29th AIAA, Fluid Dynamics Conference, Fluid Dynamics and Co-located Conferences*, Minneapolis, Albuquerque, U.S.A., 1998.
[36] Wilcox, D. C., Formulation of the k-ω Turbulence Model Revisited, *AIAA Journal*, 46(11), 2008, pp. 2823-2838.
[37] MacCormack, R. W., Candler, G.V., The Solution of Navier-Stokes Equations Using Gauss-Siedal Line Relaxation, *Computers and Fluids*, 17(1), 1989, pp. 135-150.
[38] Wright, M. J., Candler, G. V., Bose, D., Data-Parallel Line Relaxation Method for the Navier-Stokes Equations, *AIAA Journal*, 36(9), 1998, pp. 1603-1609.
[39] Sinha, K., Mahesh, K., Candler, G. V., Modeling the Effect of Shock-Unsteadiness in Shock Turbulent Boundary-Layer Interactions, *AIAA Journal*, 43(3), 2005, pp. 586-594.
[40] Pasha, A. A., Sinha, K., Shock-Unsteadiness Model Applied to Oblique Shock Wave/Turbulent Boundary-Layer Interaction, *International Journal of Computational Fluid Dynamics*, 22(8), 2008, pp. 569-582.
[41] Pasha, A.A., Sinha, K., Shock Unsteadiness Model Applied to Hypersonic Shock Wave Turbulent Boundary-Layer Interactions, *Journal of Propulsion and Power*, 28(1), 2012, pp. 46-60.
[42] Menter, F. R., Two-Equation Eddy-Viscosity Turbulence Models for Engineering Applications, *AIAA Journal*, 32(8), 1994, pp. 1598-1605.